Chemical Science

EDGE ARTICLE

Check for updates

All publication charges for this article have been paid for by the Royal Society of Chemistry

A cyclic trinuclear silver complex for photosynthesis of hydrogen peroxide†

Ri-Qin Xia, [ID] Zhen-Na Liu, Yu-Ying Tang, Xiao Luo, Rong-Jia Wei, [ID] Tao Wu, [ID] Guo-Hong Ning [ID] * and Dan Li [ID] *

The development of metal complexes for photosynthesis of hydrogen peroxide (H_2O_2) from pure water and oxygen using solar energy, especially in the absence of any additives (*e.g.*, acid, co-catalysts, and sacrificial agents), is a worthwhile pursuit, yet still remains highly challenging. More importantly, the O_2 evolution from the water oxidation reaction has been impeded by the classic bottleneck, the photon-flux-density problem of sunlight that could be attributed to rarefied solar radiation for a long time. Herein, we reported synthesis of boron dipyrromethene (BODIPY)-based cyclic trinuclear silver complexes (Ag-CTC), and they exhibited strong visible-light absorption ability, a suitable energy bandgap, excellent photochemical properties and efficient charge separation ability. The integration of BODIPY motifs as oxygen reduction reaction sites and silver ions as water oxidation reaction sites allows Ag-CTC to photosynthesize H_2O_2 either from pure water or from sea water in the absence of any additives with a high H_2O_2 production rate of 183.7 and 192.3 $\mu M\ h^{-1}$, which is higher than that of other reported metal-based photocatalysts. The photocatalytic mechanism was systematically and ambiguously investigated by various experimental analyses and density functional theory (DFT) calculations. Our work represents an important breakthrough in developing a new Ag photocatalyst for the transformation of O_2 into H_2O_2 and H_2O into H_2O_2.

Introduction

Hydrogen peroxide (H_2O_2), an environment-friendly oxidant and a clean fuel is widely used in medical disinfection, water treatment and chemical synthesis,[1-10] with an annual demand of 5.7 million tons by 2027.[11] So far, the anthraquinone oxidation process is still the most used approach for H_2O_2 production in industry; however, it requires expensive palladium catalysts and a large amount of harmful organic solvent and consumes lots of energy.[12] Therefore, it is a worthwhile pursuit to develop green and efficient catalysts, especially solar photocatalysts, for H_2O_2 production from water and oxygen due to its potential for solving global energy shortage and ecological issues.

Artificial photosynthesis of H_2O_2 using metal complexes (MCs) requires several processes including light absorption, charge-separation, the water oxidation reaction (WOR) and the oxygen reduction reaction (ORR). Currently, the ORR half-reaction has been predominantly investigated for photosynthesis of H_2O_2; however, the WOR half-reaction is not sufficiently exploited,[13-17] which severely hindered practical application. This because the WOR process suffers from

College of Chemistry and Materials Science, Guangdong Provincial Key Laboratory of Supramolecular Coordination Chemistry, Jinan University, Guangzhou 510632, People's Republic of China. E-mail: guohongning@jnu.edu.cn; danli@jnu.edu.cn

sluggish kinetics, the so called "photo-flux-density problem of sunlight",[18,19] especially for the photocatalytic four-electron (4e⁻) oxygen evolution reaction (OER). Typically, the generation of O_2 photo-catalysis by MCs takes seconds, which is far longer than the timescale for hole generation and migration.[18,19] During this long period, the photocatalyst would undergo undesired decomposition or transformation, leading to a loss of catalytic activity. Therefore, it is a worthwhile pursuit to develop MCs that are capable of photo-catalyzing both the ORR and WOR, yet it still remains highly challenging.

Conventionally, to bypass the WOR issues, hybrid catalytic systems involving two or more different components are designed (Scheme 1a).[11,12,20-22] For instance, Ru or Cu complexes as photocatalysts or photosensitizers for the 2e⁻ ORR, and Co/Ir complexes or semiconductors (*i.e.*, WO_3 or $BiVO_4$) as water oxidation catalysts (WOCs) are combined for producing H_2O_2.[11,23-28] Moreover, the addition of sacrificial agents, a superoxide anion radical ($O_2^{\cdot-}$) stabilizer (*i.e.*, $Sc(NO_3)_3$) and a proton source (*e.g.*, H_2SO_4 or $HClO_4$) is required in these homogeneous catalytic systems. Thus, these processes not only produce by-products and harmful waste, but also require additional purification steps. Furthermore, low visible-light absorption ability of reported MCs, decomposition of H_2O_2 triggered by MCs, and the unsatisfactory H_2O_2 production performance also remains unresolved problems in this field.

(a) Previous works: hybrid catalytic systems

(b) This work: integrated system
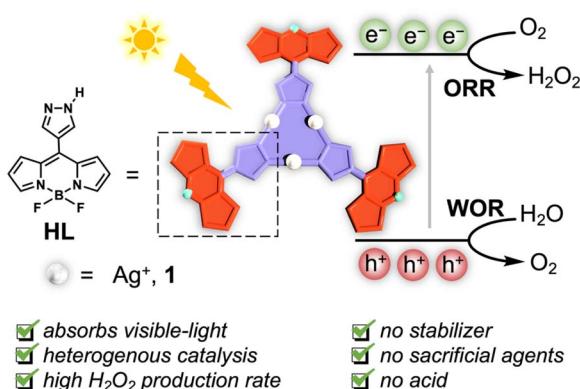
Scheme 1 Schematic illustration of (a) conventional metal-based hybrid catalytic systems and (b) a Ag-CTC complex in this work for photosynthesis of H_2O_2. (ORC and WOC mean the oxygen reduction catalyst and water oxidation catalyst).

More importantly, these photocatalytic systems did not address the WOR bottleneck.

Recently, great efforts have been put into developing transition MCs with strong visible-light absorption, which can be used in photocatalytic oxidation, and hydrogen evolution from water.[29–32] For instance, the incorporation of boron dipyrromethene (BODIPY) into a cyclic trinuclear copper(I) complex (Cu-CTC) has significantly improved its visible-light absorption, leading to light-induced $O_2^{\cdot-}$ generation from molecular oxygen (O_2). Since $O_2^{\cdot-}$ is involved in one of the reaction pathways for photosynthesis of H_2O_2 (see eqn (1)–(5)), we hypothesize that BODIPY-based CTCs might be promising photocatalysts for H_2O_2 production and address the above-mentioned issues.

Herein, we rationally designed BODIPY-based Ag-CTC (Ag_3L_3, **1**) and Cu-CTC (Cu_3L_3, **2**) by complexation between a BODIPY-based pyrazolyl ligand (**HL**) and silver benzoate (PhCOOAg) or $Cu(NO_3)_2$, respectively (Scheme 1b). For comparison, $Ag_3L^1_3$ (**3**, HL^1 represents 3,5-bis(trifluoromethyl)-1*H*-pyrazole) as a reference compound was also synthesized.[33] The incorporation of the BODIPY motif remarkably improved the photophysical properties of **1** and **2**, and they both featured high molar absorptivity ($\varepsilon = {\sim}7.4$ and 7.9×10^4 M^{-1} cm^{-1}), and good photo-induced charge-separation efficiency in the visible-light range. Under light irradiation, Ag-CTC **1** as a heterogenous photocatalyst delivered a high H_2O_2 production rate of 183.7 μM h^{-1} in the absence of a co-catalyst, sacrificial agents and acid, and it performed better than **HL**, Cu-CTC **2** and reference compound **3**. Notably, to the best of our knowledge, Ag-CTC **1** is

the best metal complex-based photocatalyst for H_2O_2 production to date. The mechanistic studies further revealed that Ag-CTC **1** can generate H_2O_2 through a stepwise e^- ORR pathway (*i.e.*, $O_2 \rightarrow O_2^{\cdot-} \rightarrow H_2O_2$), and we unexpectedly found that the holes generated after visible-light irradiation can be used to perform the oxygen evolution reaction (OER). The $4e^-$ WOR occurred at the silver center. Our work, for the first time, has demonstrated that molecular metal complexes composed of oxygen reduction and oxidation centers can be used in the full reaction photosynthesis of H_2O_2 without sacrificial agents.

$$O_2 + 2H^+ + 2e^- \rightarrow H_2O_2, (E^\theta = +0.68 \text{ V } vs. \text{ NHE}) \quad (1)$$

$$O_2 + e^- \rightarrow O_2^{\cdot-}, (E^\theta = -0.33 \text{ V } vs. \text{ NHE}) \quad (2)$$

$$O_2^{\cdot-} + 2H^+ + e^- \rightarrow H_2O_2, (E^\theta = +1.44 \text{ V } vs. \text{ NHE}) \quad (3)$$

$$2H_2O + 4h^+ \rightarrow O_2 + 4H^+, (E^\theta = +1.23 \text{ V } vs. \text{ NHE}) \quad (4)$$

$$2H_2O + 2h^+ \rightarrow H_2O_2 + 2H^+, (E^\theta = +1.76 \text{ V } vs. \text{ NHE}) \quad (5)$$
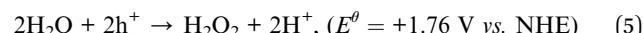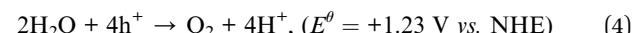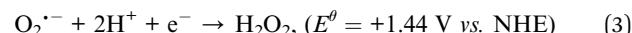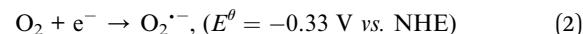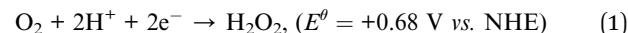
Results and discussion

Synthesis and characterization

The BODIPY-based pyrazolyl ligand (**HL**) was prepared according to our previous work.[29] The mixture of **HL** and PhCOOAg in anhydrous THF solution was stirred for 24 hours in the dark at room temperature (rt) to give compound **1** as an orange powder (Scheme S1†). The structure of **1** was characterized by using ^{1}H, ^{19}F, and ^{13}C NMR spectra (Fig. S1–S3†). The disappearance of the N–H signal of ligand **HL** at 13.81 ppm suggested the deprotonation of **HL** and formation of Ag–N bonds. The ^{19}F NMR spectra of **1** and **HL** revealed that they both display one ^{19}F peak located at −141.89 and −141.66 ppm, respectively, further proving the purity of **1**. The X-ray photoelectron spectroscopy (XPS) measurement of 1 showed intensely sharp and symmetrical Ag(I) $2d_{3/2}$ and $2d_{5/2}$ peaks at 374.09 and 368.10 eV, respectively (Fig. S5†). Energy-dispersive X-ray spectroscopy (EDS) elemental mapping confirmed that Ag, C, N, B, and F elements were evenly distributed in **1** (Fig. S6†). The orange crystals suitable for single-crystal X-ray diffraction (SXRD) analysis can be obtained with a yield of 13.7% by the solvothermal synthesis method.[34]

As shown in Fig. 1, **1** was crystalized in the $Ia\bar{3}$ cubic space group, exhibiting nine-membered Ag_3N_6 units with a distorted planar structure (Fig. 1a). The dihedral angle between the Ag_3N_6 plane and the BODIPY unit is ∼31°, leading to a propeller-shaped structure with three blades (Fig. 1a). In addition, two Ag-CTCs tightly stacked with each other to form a dimer with an interdimer Ag···Ag distance of 3.75 Å (Fig. 1b), revealing strong Ag–Ag interactions. Reference compound Cu-CTC **2** (ref. 29) and $Ag_3L^1_3$ **3** (ref. 35 and 36) were synthesized for comparison and their crystal structures are shown in Fig. 1c and d, respectively. They both exhibited similar nine-membered planar configurations. Furthermore, thermo-gravimetric analysis (TGA) of **1** revealed that it started to decompose at 260 °C (Fig. S9†). The phase purity of **1** was confirmed by powder X-ray diffraction
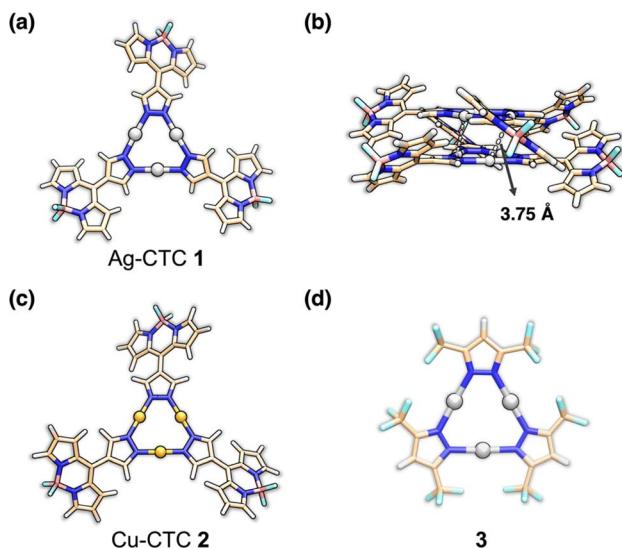
Fig. 1 Crystal structures of (a) Ag-CTC **1**, (c) Cu-CTC **2** and (d) $Ag_3L^1_3$ **3**, exhibiting one CTC unit structure. (b) Side view of tightly packed **1** showing an interdimer Ag⋯Ag distance of 3.75 Å (ball–stick model) (color codes: C, wheat; N, blue; Cu, orange; Ag, silver; B, light pink; and F, light green).

(PXRD) (Fig. S10†). The water contact angles of **HL**, **1**, **2** and **3** are all larger than 110°, suggesting that they are all hydrophobic (Fig. S13†).

Optics and electrochemistry

The UV-vis absorption spectra of **1** exhibited strong adsorption at 497 nm with an exceptionally high molar extinction coefficient (ε) of 74 353 M^{-1} cm^{-1} (Fig. S16 and S17†). This value is similar to that of compound **2** ($\varepsilon = 78\,515$ M^{-1} cm^{-1}) and approximately 5.17 times higher than that of **HL** ($\varepsilon = 14\,379$ M^{-1} cm^{-1}).[13] In addition, the solid-state UV-vis diffuse reflection spectra of **HL**, **1**, **2** and **3** were obtained to study light absorption ability. Specifically, **2** exhibited the widest absorption range (i.e., 200–800 nm), while **3** showed the narrowest absorption range (i.e. 200–400 nm) (Fig. 2a). **HL** and **1** delivered similar absorption edges at ~600 nm. These results suggested that the incorporation of BODIPY units remarkably improved visible-light harvesting ability of CTCs. The optical bandgaps (E_g) of **HL**, **1**, **2** and **3** were estimated to be 1.97, 2.16, 1.76 and 2.94 eV, respectively by using the Tauc plot (Fig. 2b). The flat band potentials of **HL**, **1**, **2** and **3** were determined to be −1.38, −0.80, −1.33 and −1.47 eV vs. NHE at pH = 7 through the Mott–Schottky experiments,[37] respectively (Fig. S18–S21†), which were equal to their conduction band (CB) potentials. Combining the Mott–Schottky experiments and optical bandgap data, valence band (V_B) potentials of **HL**, **1**, **2** and **3** were calculated to be 0.59, 1.36, 0.43 and 1.47 eV vs. NHE at pH = 7 (Fig. 2c). Since the reduction potentials of $O_{2(g)}/O_2^{\cdot-}$ and $O_{2(g)}/H_2O_2$ are known to be −0.35 and 0.28 V vs. NHE at pH = 7,[38] they are thermodynamically suitable for photocatalytic reduction of O_2 to give H_2O_2. In addition, the oxidation potential of H_2O/O_2 is 0.82 V vs. NHE at pH = 7;[39] thus, compounds **1** and **3** are

thermodynamically suitable for photocatalytic oxidation of water to produce O_2 and protons.

To further probe the optical and photo-electrochemical properties of **HL**, **1**, **2** and **3**, photoluminescence (PL) spectra were obtained, and electrochemical impedance spectroscopy (EIS) and transient photocurrent measurements were performed. The steady-state PL spectra of **HL**, **1**, **2** and **3** in the suspended-state were obtained (Fig. 2d). **HL**, **1** and **2** showed bright green emission with maximum emission peak (λ_{em}) positions at 514 nm, while the emission intensity of **3** was very weak (Fig. S24–S28†). Compounds **1** and **2** exhibited similar emission intensity, much lower than that of **HL**, suggesting that **1** and **2** possessed the highest separation efficiency of photo-induced electron–hole pairs and the presence of electron transfer.[40] Moreover, **2** possessed the highest photocurrent density, while the transient photocurrent density of **1** was larger than that of **HL** and **3** under visible-light irradiation, implying an effective spatial separation of photogenerated charge carriers in **1** and **2** (Fig. 2e). The EIS spectra of **HL**, **1**, **2** and **3** exhibited semicircles; meanwhile **1** and **2** delivered the lowest charge transfer resistance (Fig. 2f), indicating the highest charge-separation efficiency in **1** and **2**.

Photosynthesis of H_2O_2

The visible-light photosynthesis of H_2O_2 was initially tried in pure water under an O_2 atmosphere and the yield of H_2O_2 was determined by iodometric titration.[41] The production rate of H_2O_2 with different amounts of photocatalyst **1** (i.e. 1, 2, 3, 4 and 5 mg) in 5 mL pure water was measured. It was found that 4 mg of **1** furnished the highest H_2O_2 production rate of 229.7 μmol g^{-1} h^{-1} (Fig. S33†). Fig. 3a shows the photocatalytic performances of **HL**, **1**, **2** and **3**, and a linear relationship between H_2O_2 production and irradiation time was observed under optimal conditions. With compound **1**, the concentration of H_2O_2 gradually increased to 918.5 μM after 5 hours, and the production rate was estimated to be 183.7 μM h^{-1} (Fig. 3a). In sharp contrast, when **HL**, **2** and **3** were employed as photocatalysts, no H_2O_2 was detected (Fig. 3a). Notably, although Cu-CTC **2** exhibited better photoinduced charge separation efficiency than Ag-CTC **1**, **2** was not able to produce H_2O_2 under light irradiation. This is because H_2O_2 decomposition is catalyzed by **2** (Fig. S35†), which has also observed for other reported Cu-CTC complexs.[42] In addition, the unsuitable bandgaps of **HL**, and **2** for the 4e⁻ WOR also hampered the photosynthesis of H_2O_2. Moreover, although Ag-CTC **3** had a suitable optic bandgap, the low light absorption ability impeded the photoproduction of H_2O_2.

The long-term photostability of catalysts is practically important; thus, the continuous photosynthesis of H_2O_2 was conducted. In a continuous experiment (Fig. 3b), the H_2O_2 production rate leveled off after about 15 h using **1**. The amount of H_2O_2 produced under pure O_2 (99%) was 6.7 times greater than that in air, and no H_2O_2 was detected under a continuous Ar atmosphere, suggesting that O_2 is essential for H_2O_2 production (Fig. 3c and see the ESI† for details). The apparent quantum yield (AQY) of **1** was measured determined to be
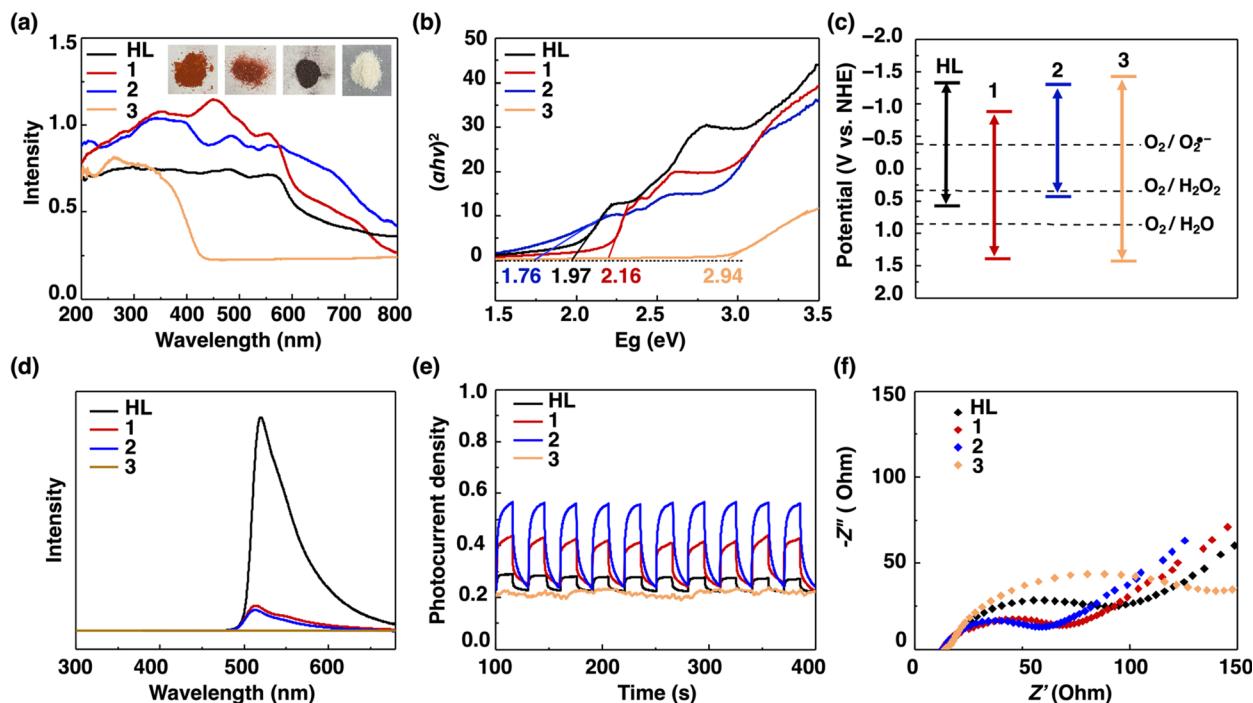
Fig. 2 (a) The solid-state UV-vis diffuse reflectance spectra of HL, 1, 2 and 3. The inset shows the photographs of powder samples of HL, 1, 2 and 3. (b) The Tauc plot curves of HL, 1, 2 and 3. (c) Energy level diagrams of HL, 1, 2 and 3. (d) PL spectra of HL, 1, 2 and 3. (e) Photocurrent response curves of HL, 1, 2 and 3 (the unit is μA cm^{-1}). (f) Nyquist plots of HL, 1, 2 and 3.
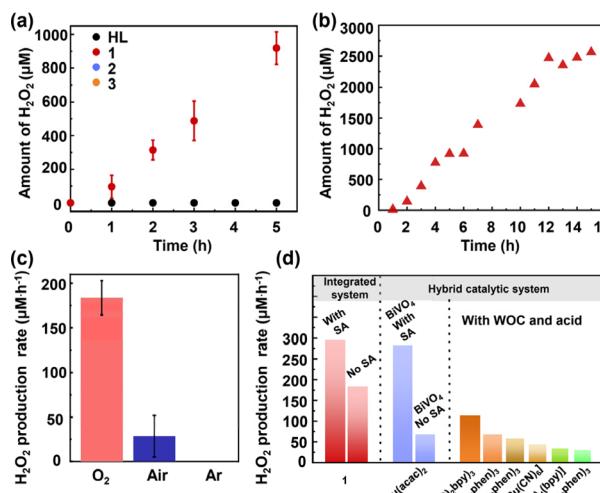

Fig. 3 (a) Time course of photocatalytic H$_2$O$_2$ production for HL, 1, 2 and 3 irradiated with a 300 W xenon lamp fitted with a λ > 420 nm filter. (b) Long-term photocatalytic H$_2$O$_2$ production of 1. (c) Photocatalytic H$_2$O$_2$ production activities of 1 under different gas atmospheres. (d) Comparison of the H$_2$O$_2$ production rate with representative metal-based photocatalysts. The error bars denote ±s.d. of the mean for three independent experiments in (a) and (c).

0.039%, 0.043%, 0.035%, 0.040% and 0.042% at 420, 450, 485, 520 and 535 nm, respectively (Fig. S38†), suggesting a visible-light promoted H$_2$O$_2$ production process. Compared to pure water, sea water is the most earth-abundant resource. Thus,

photosynthesis of H$_2$O$_2$ from sea water is highly desired, yet is a significant challenge due to the complex composition and high salt concentration of seawater. Interestingly, 1 demonstrated an even higher H$_2$O$_2$ photo-production rate of 192.3 μM h^{-1} using seawater (Fig. S40 and S41†). Notably, 1 delivered the highest H$_2$O$_2$ production rate among reported metal-based photocatalysts (Fig. 3d).[23,25,43–47] These results indicate that 1 is a promising photocatalyst for H$_2$O$_2$ production. However, with the increase in photo-generated holes and concentration of H$_2$O$_2$, the photo-catalytic performance decreased after 15 h of photo-irradiation, and the crystallinity of 1 declined as confirmed by PXRD analysis (Fig. S42†). These results suggested the moderate stability and durability of complex 1 during photosynthesis of H$_2$O$_2$. Nevertheless, our work presented a rare example of a Ag complex for photo-catalyzing both the ORR and OER.

To reveal the photocatalytic mechanism, several control experiments were conducted. Firstly, the H$_2$O$_2$ production rate increased to 237.8 μM h^{-1} with tert-butanol (TBA) as the sacrificial agent. The enhancement of the H$_2$O$_2$ production rate in the presence of TBA as electron donors indicated that ˙OH did not participate in the H$_2$O$_2$ production reaction (Fig. 4a).[48] Secondly, the addition of AgNO$_3$ as electron acceptors significantly decreased the H$_2$O$_2$ production rate to 30.5 μM h^{-1}, indicating that photogenerated electrons played a vital role in the photocatalytic ORR. Thirdly, in the presence of La$_2$O$_3$, NaIO$_3$ and 1 in pure water, O$_2$ was detected and the production rate was estimated to be 81.8 μmol g^{-1} h^{-1} after 5 h of photo-irradiation (Table S3 and Fig. S44, S45†). This observation
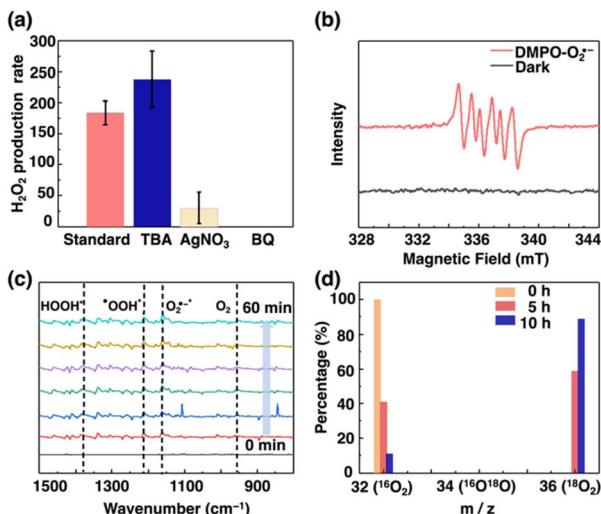
Fig. 4 (a) Photocatalytic H_2O_2 production activities of **1** with the addition of different sacrificial agents (the unit is $\mu M\ h^{-1}$). The error bars denote ±s.d. of the mean for three independent experiments. (b) EPR trapping experiments in the presence of DMPO before (gray line) and after (light red line) light irradiation. (c) *In situ* DRIFT spectra of **1** during H_2O_2 photosynthesis (the time interval is 10 min). (d) Isotopic $^{18}O_2$ labeling experiments.

suggests that Ag-CTC **1** is able to directly photo-produce O_2 from water through the $4e^-$ OER. To further prove that O_2 was photogenerated from water, the $H_2^{18}O$ isotopic labeling experiment was conducted.[49,50] As shown in Fig. S46,† in the presence of $^{16}O_2$ and $H_2^{18}O$, the reaction mixture was irradiated after 12 hours. Afterward, the resulting solution was decomposed by MnO_2, and $^{18}O_2$ was observed by mass spectroscopy, indicating that $H_2^{18}O$ participated in the OER to generate $^{18}O_2$, and the generated $^{18}O_2$ was further captured in the ORR to convert $H_2^{18}O_2$. Finally, the addition of *p*-benzoquinone (BQ) as an $O_2^{\cdot-}$ scavenger[51] completely inhibited H_2O_2 production (Fig. 4a), suggesting that $O_2^{\cdot-}$ was required during the photosynthesis of H_2O_2. These results are consistent with the observed optical properties of **1**. For instance, the CB and VB of **1** also suggested that the $2e^-$ ORR (*i.e.*, O_2 to H_2O_2) and $4e^-$ WOR (*i.e.*, H_2O to O_2) are thermodynamically possible, while e^- (*i.e.*, H_2O to $\cdot OH$) and $2e^-$ WOR (*i.e.*, H_2O to H_2O_2) are thermodynamically prohibited.

To further study the reaction pathway of H_2O_2 production by Ag-CTC **1**, the average electron transfer number of Ag-CTC **1** was determined to be 2.00 based on the results of rotating disc electrode (RDE) studies conducted on O_2 reduction processes (Fig. S47†), which showed that Ag-CTC **1** could reduce O_2 to H_2O_2 using the direct two-electron reduction pathway. Meanwhile, 5,5-dimethyl-1-pyrroline *N*-oxide (DMPO) was employed as the radical trapping agent for detecting $O_2^{\cdot-}$ in electron paramagnetic resonance (EPR) measurements. No noticeable signals can be found under dark conditions, while the characteristic signals of DMPO-$O_2^{\cdot-}$ appeared after light irradiation (Fig. 4b).[52] Such results further supported the generation of $O_2^{\cdot-}$ though the one-electron reduction of O_2. In addition, the adsorbed intermediates on **1** during the H_2O_2 production process were revealed by *in situ* diffuse reflectance infrared

Fourier transform spectroscopy (DRIFTS). As shown in Fig. 4c, the O–O stretching signals for O_2 as well as $O_2^{\cdot-}*$, $\cdot OOH*$, and $HOOH*$ (* denoted as surface-adsorbed) were found at 954, 1160, 1211 and 1379 cm^{-1}, respectively.[53–55] Moreover, isotopic labeling experiments using $^{18}O_2$ were also performed. The percentage of $^{18}O_2$ detected by mass spectroscopy increased from 0% to 88.2% over 5 h and further decreased to 75.3% after 10 h (Fig. 4d), suggesting that the $^{16}O_2$ generated by the OER would be captured in the ORR and converted into $H_2^{16}O_2$. Such results are consistent with the $H_2^{18}O$ isotopic labeling experiment, and reveal that the photosynthesis of H_2O_2 using Ag-CTC **1** involves stepwise ORR (*i.e.*, $O_2 \rightarrow O_2^{\cdot-} \rightarrow H_2O_2$)[56] and the $4e^-$ OER process (*i.e.*, $H_2O \rightarrow O_2$).

Theoretical studies

Density functional theory (DFT) calculations were conducted by Gaussian 09E (ref. 57) software to further study the reaction mechanism. The electrostatic potential (ESP)[58,59] distribution is used to describe the charge distribution on the surface of molecule **1** (Fig. S53†). The electrostatic potential value surrounding the BODIPY moiety has a negative value, while the nine-membered Ag_3N_6 unit exhibits a positive value, suggesting that the BODIPY region has a higher affinity for electrons and is more electrophilic compared to the nine-membered Ag_3N_6 unit.[60] Thus, the electrons prefer to be transferred from the Ag_3N_6 unit to the BODIPY motifs.[1] In addition, the cyclic voltammetry (CV) test was performed to study their redox potentials. The CV curve of **1** exhibited two reversible redox processes with the peak potential at approximately −1.65 and −1.26 V (*vs.* $Fc^{+/0}$), respectively, which can be assigned to the redox couple of Ag^{II}/Ag^{I}, and the BODIPY ligands (Fig. S52†). The more negative reduction potential of the Ag center compared to that of BODIPY ligands further suggests that the electron transfer process from the Ag to BODIPY unit is thermodynamic feasible.[61] Moreover, as shown in Fig. 5a, the electrons were primarily localized at the BODIPY units either in the highest occupied or lowest unoccupied molecular orbital (HOMO or LUMO). According to the time-dependent density-functional theory (TDDFT) calculation results, it is indicated that BODIPY units contribute more in the transition from the ground state (S_0) to the first 10 S_n states with an *f* larger than 0.01 (Table S4†). This further confirms that for **1**, the electrons are mainly localized on the BODIPY units. Based on the above discussion, we propose that the mechanism for H_2O_2 production involves the ORR occurring on BODIPY, while the WOR takes place on the Ag_3N_6 unit.

For the ORR process, a plausible reaction mechanism is proposed in Fig. 5b. The adsorption energy (ΔE_{ad}) of O_2 in the BODIPY region of **1** and **2** was calculated to be 0.2469 and 0.2709 eV, respectively (Fig. S55–S58 and Table S5†), suggesting that the adsorption of O_2 either on **1** or **2** is thermodynamically infeasible. Nevertheless, the more negative ΔE_{ad} value of **1** compared to **2** indicates that O_2 prefers to be absorbed on **1** (Fig. 5c). It is well known that the formation of the $\cdot OOH$ intermediate is a crucial step during the synthesis of H_2O_2;[55,62,63] thus the Gibbs free energy of the $\cdot OOH$ intermediate (ΔG_{OOH*})
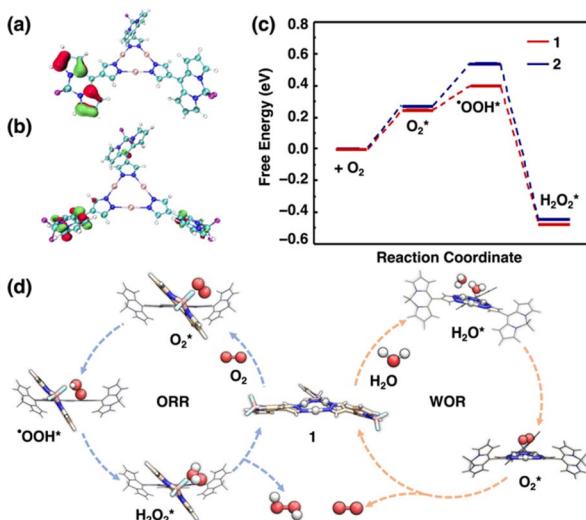
Fig. 5 (a) HOMO and (b) LUMO of **1** in the optimized structure (isovalue = 0.05 a.u.). (c) Calculated free energy for H_2O_2 formation from O_2 at the DFT-D3 (BJ) level of theory. (d) The proposed photocatalytic mechanism for H_2O_2 synthesis in the presence of photocatalyst **1** (* denoted as surface-adsorbed).

adsorbed in the BODIPY region for **1** (*i.e.*, 0.1502 eV) and **2** (*i.e.*, 0.2664 eV) is assessed and compared (Fig. 5c). The more negative value of ΔG_{OOH*} for **1** suggests that **1** is more active for ˙OOH intermediate production. Furthermore, the negative value of $\Delta G_{H_2O_2}$ (−0.8719 eV) produced on the BODIPY unit for **1** (Fig. 5c) implies that the production of H_2O_2 from the ˙OOH intermediate is thermodynamically favored.

For the $4e^-$ WOR process, two H_2O molecules are required to be adsorbed on the surface of the catalysts to produce one O_2. Based on the above-mentioned results, the WOR possibly takes place on the Ag_3N_6 unit of **1**.[64] The ΔE_{ad} of the two H_2O molecules on the Ag_3N_6 active site of **1** was also calculated to be −0.3806 eV (Fig. S59 and S60†), further evidencing that the adsorption of H_2O on the Ag_3N_6 unit of **1** is thermodynamically favored. We calculated the energy path for water oxidation into oxygen. Based on the experimental results and calculation, a possible mechanism is proposed (Fig. 5d): initially, O_2 is adsorbed on the BODIPY sites. After light irradiation, photo-induced electrons are produced at the BODIPY site, and then O_2 obtains the electron and proton to generate the ˙OOH intermediate. Afterward, ˙OOH further obtains the electron and proton to produce H_2O_2. Meanwhile, two H_2O molecules can be absorbed on the Ag_3N_6 site, and then photoinduced holes obtain electrons from H_2O to produce O_2 and protons.

Conclusions

In summary, we have prepared BODIPY decorated Ag-CTC **1**, and it features a suitable energy bandgap, strong visible-light absorption, excellent photochemical properties and efficient charge separation ability. Owing to these merits, complex **1** can be used as a photocatalyst for producing H_2O_2 either from pure water or from sea water with high photocatalytic activities (183.7 and 192.3 μM h^{-1}) in the absence of any additives (*e.g.*, acid, co-

catalysts, and sacrificial agents). The photocatalytic performance is attributed to the prominently enhanced two-electron ORR by forming endoperoxide at the BODIPY unit and highly concentrated holes at the Ag_3N_6 site. The generated O_2 from the OER is subsequently consumed by the ORR, thereby boosting overall reaction kinetics. The photocatalytic mechanism was systematically investigated by various experimental analyses and DFT calculations. Our studies demonstrated that the integration of organic chromophores as ORR sites and silver centers as OER sites is a new approach for design of efficient metal-based photocatalysts for H_2O_2 production using solar energy.

Data availability

The data supporting this article have been included as part of the ESI.† Crystallographic data for complex **1** has been deposited at the CCDC (DOI: **https://doi.org/10.5517/ccdc.csd.cc2gqh2s**) and can be obtained from **https://www.ccdc.cam.ac.uk**.

Author contributions

Conflicts of interest

The authors declare no conflict of interest.

Acknowledgements

Notes and references

1 J. N. Chang, J. W. Shi, Q. Li, S. Li, Y. R. Wang, Y. Chen, F. Yu, S. L. Li and Y. Q. Lan, *Angew. Chem., Int. Ed.*, 2023, **135**, e202303606.

2 J.-N. Lu, L. J.-J. Liu, L.-Z. Dong, J.-M. Lin, F. Yu, J. Liu and Y.-Q. Lan, *Angew. Chem., Int. Ed.*, 2023, **62**, e202308505.

3 J.-Y. Yue, L.-P. Song, Y.-F. Fan, Z.-X. Pan, P. Yang, Y. Ma, Q. Xu and B. Tang, *Angew. Chem., Int. Ed.*, 2023, **62**, e202309624.

4 Y. Zhang, C. Pan, G. Bian, J. Xu, Y. Dong, Y. Zhang, Y. Lou, W. Liu and Y. Zhu, *Nat. Energy*, 2023, **8**, 361–371.

5 W. Zhao, P. Yan, B. Li, M. Bahri, L. Liu, X. Zhou, R. Clowes, N. D. Browning, Y. Wu and J. W. Ward, *J. Am. Chem. Soc.*, 2022, **144**, 9902–9909.

6 J. Liu, Y. Zou, B. Jin, K. Zhang and J. H. Park, *ACS Energy Lett.*, 2019, **4**, 3018–3027.

7 K. Sato, M. Aoki and R. Noyori, *Science*, 1998, **281**, 1646–1647.

8 R. J. Lewis, K. Ueura, X. Liu, Y. Fukuta, T. E. Davies, D. J. Morgan, L. Chen, J. Qi, J. Singleton and J. K. Edwards, *Science*, 2022, **376**, 615–620.

9 Y. Sun, L. Han and P. Strasser, *Chem. Soc. Rev.*, 2020, **49**, 6605–6631.

10 Y. Kondo, Y. Kuwahara, K. Mori and H. Yamashita, *Chem*, 2022, **8**, 2924–2938.

11 X. Zeng, Y. Liu, X. Hu and X. Zhang, *Green Chem.*, 2021, **23**, 1466–1494.

12 J. M. Campos-Martin, G. Blanco-Brieva and J. L. G. Fierro, *Angew. Chem., Int. Ed.*, 2006, **45**, 6962–6984.

13 F. Kuttassery, Y. Ohsaki, A. Thomas, R. Kamata, Y. Ebato, H. Kumagai, R. Nakazato, A. Sebastian, S. Mathew, H. Tachibana, O. Ishitani and H. Inoue, *Angew. Chem., Int. Ed.*, 2023, **135**, e202308956.

14 T. J. Meyer, M. V. Sheridan and B. D. Sherman, *Chem. Soc. Rev.*, 2017, **46**, 6148–6169.

15 Y. Kou, Y. Nabetani, D. Masui, T. Shimada, S. Takagi, H. Tachibana and H. Inoue, *J. Am. Chem. Soc.*, 2014, **136**, 6021–6030.

16 L. Sun, *Science*, 2015, **348**, 635–636.

17 F. Zhou, C. McDonnell-Worth, H. Li, J. Li, L. Spiccia and D. R. Macfarlane, *J. Mater. Chem. A*, 2015, **3**, 16642–16652.

18 H. Inoue, T. Shimada, Y. Kou, Y. Nabetani, D. Masui, S. Takagi and H. Tachibana, *ChemSusChem*, 2011, **4**, 173–179.

19 F. Kuttassery, S. Mathew, S. N. Remello, A. Thomas, K. Sano, Y. Ohsaki, Y. Nabetani, H. Tachibana and H. Inoue, *Coord. Chem. Rev.*, 2018, **377**, 64–72.

20 S. Fukuzumi, Y. M. Lee and W. Nam, *ChemCatChem*, 2018, **10**, 9–28.

21 C. Qin, X. Wu and L. Tang, *Angew. Chem., Int. Ed.*, 2024, **136**, e202402297.

22 H. Yu, F. Zhang and Q. Chen, *Nat. Commun.*, 2023, **14**, 5238–5250.

23 S. Kato, J. Jung, T. Suenobu and S. Fukuzumi, *Energy Environ. Sci.*, 2013, **6**, 3756–3764.

24 K. Mase, M. Yoneda, Y. Yamada and S. Fukuzumi, *Nat. Commun.*, 2016, **7**, 11470.

25 T. Suenobu, S. Shibata and S. Fukuzumi, *Inorg. Chem.*, 2016, **55**, 7747–7754.

26 Y. Wang, Y. Wang, J. Zhao, M. Chen, X. Huang and Y. Xu, *Appl. Catal. B*, 2021, **284**, 119691.

27 L. Wang, J. Zhang, Y. Zhang, H. Yu, Y. Qu and J. Yu, *Small*, 2022, **18**, 2104561.

28 H. Hou, X. Zeng and X. Zhang, *Angew. Chem., Int. Ed.*, 2020, **59**, 17356–17376.

29 K. C. Chong, C. Li and B. Liu, *CCS Chem.*, 2023, **5**, 2436–2447.

30 J. Wang, J. Zhang, S. B. Peh, G. Liu, T. Kundu, J. Dong, Y. Ying, Y. Qian and D. Zhao, *Sci. China: Chem.*, 2020, **63**, 192–197.

31 R.-Q. Xia, J. Zheng, R.-J. Wei, J. He, D.-Q. Ye, G.-H. Ning and D. Li, *Inorg. Chem. Front.*, 2022, **9**, 2928–2937.

32 K. K. Chen, S. Guo, H. Liu, X. Li, Z. M. Zhang and T. B. Lu, *Angew. Chem., Int. Ed.*, 2020, **59**, 12951–12957.

33 H. R. Dias, S. A. Polach and Z. Wang, *J. Fluor. Chem*, 2000, **103**, 163–169.

34 R.-Q. Xia, Z.-N. Liu, Y.-Y. Tang, X. Luo, R.-J. Wei, T. Wu, G.-H. Ning and D. Li, *Experimental Crystal Structure Determination*, 2024, DOI: **10.5517/ccdc.csd.cc2gqh2s**.

35 O. Renn, L. M. Venanzi, A. Marletetti and V. Gramlich, *Helv. Chim. Acta*, 1995, **78**, 993–1000.

36 C. Zhu, H. Zeng, C. Liu, Y. Cai, X. Fang and H. Jiang, *Org. Lett.*, 2020, **22**, 809–813.

37 J.-K. Jin, K. Wu, X.-Y. Liu, G.-Q. Huang, Y.-L. Huang, D. Luo, M. Xie, Y. Zhao, W. Lu and X.-P. Zhou, *J. Am. Chem. Soc.*, 2021, **143**, 21340–21349.

38 W. H. Koppenol, D. M. Stanbury and P. L. Bounds, *Free Radical Biol. Med.*, 2010, **49**, 317–322.

39 L. Liu, M.-Y. Gao, H. Yang, X. Wang, X. Li and A. I. Cooper, *J. Am. Chem. Soc.*, 2021, **143**, 19287–19293.

40 H. Lin, Y. Liu, Z. Wang, L. Ling, H. Huang, Q. Li, L. Cheng, Y. Li, J. Zhou and K. Wu, *Angew. Chem., Int. Ed.*, 2022, **61**, e202214142.

41 Z. Wei, M. Liu, Z. Zhang, W. Yao, H. Tan and Y. Zhu, *Energy Environ. Sci.*, 2018, **11**, 2581–2589.

42 X. Li, J. Wang, F. Xue, Y. Wu, H. Xu, T. Yi and Q. Li, *Angew. Chem., Int. Ed.*, 2021, **60**, 2534–2540.

43 M. Teranishi, T. Kunimoto, S.-i. Naya, H. Kobayashi and H. Tada, *J. Phys. Chem. C*, 2020, **124**, 3715–3721.

44 Y. Isaka, Y. Yamada, T. Suenobu, T. Nakagawa and S. Fukuzumi, *RSC Adv.*, 2016, **6**, 42041–42044.

45 Y. Isaka, K. Oyama, Y. Yamada, T. Suenobu and S. Fukuzumi, *Catal. Sci. Technol.*, 2016, **6**, 681–684.

46 Y. Isaka, S. Kato, D. Hong, T. Suenobu, Y. Yamada and S. Fukuzumi, *J. Mater. Chem. A*, 2015, **3**, 12404–12412.

47 Y. Aratani, T. Suenobu, K. Ohkubo, Y. Yamada and S. Fukuzumi, *Chem. Commun.*, 2017, **53**, 3473–3476.

48 J. Yang, B. Pan, H. Li, S. Liao, D. Zhang, M. Wu and B. Xing, *Environ. Sci. Technol.*, 2016, **50**, 694–700.

49 D. Chen, W. Chen, Y. Wu, L. Wang, X. Wu, H. Xu and L. Chen, *Angew. Chem., Int. Ed.*, 2023, **135**, e202217479.

50 Z. Teng, Q. Zhang, H. Yang, K. Kato, W. Yang, Y.-R. Lu, S. Liu, C. Wang, A. Yamakata and C. Su, *Nat. Catal.*, 2021, **4**, 374–384.

51 Y. Wang, Y. Xie, H. Sun, J. Xiao, H. Cao and S. Wang, *ACS Appl. Mater. Interfaces*, 2016, **8**, 9710–9720.

52 J.-L. Clément, N. Ferré, D. Siri, H. Karoui, A. Rockenbauer and P. Tordo, *J. Org. Chem.*, 2005, **70**, 1198–1203.

53 J. N. Chang, Q. Li, J. W. Shi, M. Zhang, L. Zhang, S. Li, Y. Chen, S. L. Li and Y. Q. Lan, *Angew. Chem., Int. Ed.*, 2023, **62**, e202218868.

54 C. Zhao, X. Wang, Y. Yin, W. Tian, G. Zeng, H. Li, S. Ye, L. Wu and J. Liu, *Angew. Chem., Int. Ed.*, 2023, **62**, e202218318.

55 M. Kou, Y. Wang, Y. Xu, L. Ye, Y. Huang, B. Jia, H. Li, J. Ren, Y. Deng and J. Chen, *Angew. Chem., Int. Ed.*, 2022, **61**, e202200413.

56 H. Yang, C. Li, T. Liu, T. Fellowes, S. Y. Chong, L. Catalano, M. Bahri, W. Zhang, Y. Xu and L. Liu, *Nat. Nanotechnol.*, 2023, **18**, 307–315.

57 M. J. Frisch, G. W. Trucks, H. B. Schlegel, G. E. Scuseria, M. A. Robb, J. R. Cheeseman, G. Scalmani, V. Barone, B. Mennucci, G. A. Petersson, H. Nakatsuji and D. J. Fox, *Gaussian 09 (Revision E . p. 01)*, Gaussian. Inc., Wallingford, CT, 2009.

58 H. Yao, Y. Cui, D. Qian, C. S. Ponseca Jr., A. Honarfar, Y. Xu, J. Xin, Z. Chen, L. Hong, B. Gao, R. Yu, Y. Zu, W. Ma, P. Chabera, T. Pullerits, A. Yartsev, F. Gao and J. Hou, *J. Am. Chem. Soc.*, 2019, **141**, 7743–7750.

59 J. S. Murray and P. Politzer, *Rev.: Comput. Mol. Sci.*, 2017, **7**, e1326.

60 J. Zheng, Z. Lu, K. Wu, G.-H. Ning and D. Li, *Chem. Rev.*, 2020, **120**, 9675–9742.

61 G.-Y. Wang, S. Guo, P. Wang, Z.-M. Zhang and T.-B. Lu, *Appl. Catal. B*, 2022, **316**, 121655.

62 G. Han, X. Zhang, W. Liu, Q. Zhang, Z. Wang, J. Cheng, T. Yao, L. Gu, C. Du and Y. Gao, *Nat. Commun.*, 2021, **12**, 6335.

63 R. B. Rankin and J. Greeley, *ACS Catal.*, 2012, **2**, 2664–2672.

64 Y.-Y. Tang, X. Luo, R.-Q. Xia, J. Luo, S.-K. Peng, Z.-N. Liu, Q. Gao, M. Xie, R.-J. Wei, G.-H. Ning and D. Li, *Angew. Chem., Int. Ed.*, 2024, e202408186.